J. Magn. Soc. Japan, 25, 399–407 (2001)

Real-time studies of mark formation processes in phase-change and magneto-optical media using a two-laser tester

Masud Mansuripur, Pramod K. Khulbe, Xiaodong Xun, J. Kevin Erwin, and Warren Bletscher
Optical Sciences Center, The University of Arizona, Tucson, Arizona 85721

(Received October 5, 2000; Accepted December 20, 2000)

Abstract—We have equipped a commercial polarized-light microscope with two laser diodes operating at 643nm and 680 nm. The two laser beams are focused simultaneously and coincidentally on the sample through the microscope objective lens. We use one of the lasers in the pulsed mode to write marks on the sample, and the other laser in a low-power cw mode to monitor the changes in reflectivity and/or the state of polarization upon reflection from the sample. The system has a liquid crystal wave-plate for adjusting the optical phase-shifts, an electro-magnet, a hot plate, a computerized XY-stage, two polarizing beam-splitters, and both single-ended and differential detection modules for each of the laser wavelengths.

The dynamics of phase-transition (i.e., melting, crystallization, and amorphization upon rapid cooling from melt in the case of PC media, and ferrimagnetic-to-paramagnetic in the case of MO media) are readily observed in the 160 MHz-bandwidth signal picked up by the detectors. Similarly, changes in the magnetic state of the MO media under a focused spot (whether due to the change of temperature or caused by magnetization reversal), are monitored in real-time.

We describe the dynamics of phase transformation in PC media as well as the observed behavior of magnetization of the MO media within the region of the hot spot. These observations are made over periods ranging from 30 ns up to several microseconds, with a resolution of only a few nanoseconds. We also outline the methods of extracting from the observed data the physical parameters of the media such as the specific heat, thermal conductivity, temperature-dependence of the optical constants, and the probabilities of nucleation and growth.

Keywords: optical recording, phase-change media, magneto-optical media, time-resolved measurements.

1. Introduction

Optical data storage products encompass the range from read-only (CD, DVD, CD-ROM, DVD-ROM) to write-once-read-many (CD-R, DVD-R) to rewritable (magneto-optical and phase-change). The read-only media are injection molded at the factory, with the information-carrying marks embossed upon their plastic substrate. The recording process in writable and rewritable media, however, is a thermal process initiated by a focused laser beam. The focused beam raises the local temperature of the storage layer, causing in the case of phase change (PC) media a transition between amorphous and crystalline phases of the material and, in the case of magneto-optical (MO) media, a reversal of the magnetic moment within the heated spot. The local change of state is accompanied by a change in either the reflectivity of the media or the state of polarization of the reflected beam or both. One can thus investigate the physical changes that occur during the recording and erasure processes by monitoring the reflected light.

In this paper we report recent results from a static tester that has been built for analyzing the recording processes in writable and rewritable media of optical data storage. The tester is built around a commercial polarized-light microscope and contains two semi-conductor laser diodes operating at $\lambda_1 = 643$ nm and $\lambda_2 = 680$ nm. The two laser beams are brought to focus at the same spot on the storage layer of the media. While one laser provides the heat for raising the temperature and changing the local state of the sample, the other laser operates at a low cw power, probing the changes in the reflectivity of the sample (or in the state of polarization of the reflected beam) without causing any significant heating of its own. Using high-speed photodetectors, we have been able to monitor the changes in the reflected light with a temporal resolution of better than 10 ns. We have thus followed the changes that take place within the sample as a function of time both during the heating cycle and in the short interval immediately following the laser pulse, when the temperatures are appreciable and change is still in progress.

The paper is organized as follows. Section 2 provides a description of the tester's design and its principle of operation. Section 3 gives examples of the type of information that is obtained from experiments on PC media; these examples shed light on the processes of crystallization, melting, and amorphization in quadrilayer PC samples. In Section 4 we present another example of the application of the static tester, this time in analyzing the thermomagnetic recording process in a quadrilayer MO stack. Section 5 is a summary of the paper and contains a few final remarks and conclusions.

2. Design and Operation of the Static Tester

The tester is built around a commercially available polarized light microscope. A diagram of the complete system is shown in Fig. 1. The white-light source, the objective lens, the CCD camera, the polarizer, and the analyzer are standard elements of the microscope and were not modified by us in any way. We use the white-light source and the camera for direct observation of the recorded marks and for visual inspection of the samples. The components within the boxed region in Fig. 1 include the two lasers and the necessary optical and electronic elements for guiding their beams to the sample, and for

detecting the beams' properties on reflection from the sample; these items were not part of the original microscope and were added by us.

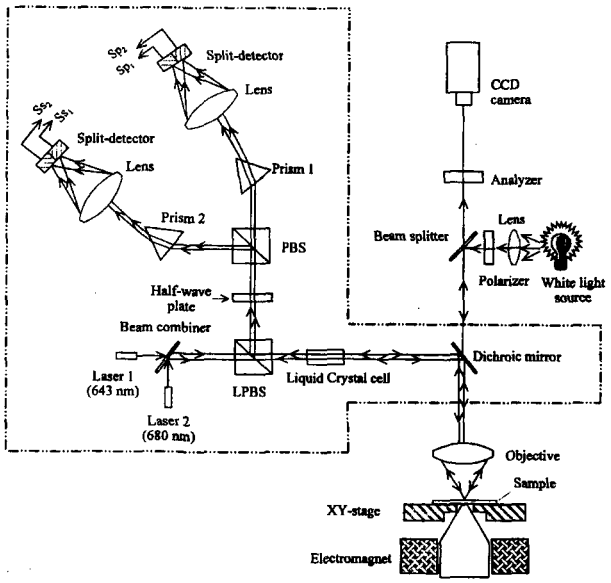

Fig. 1 Schematic diagram of the static tester

A dichroic mirror introduces the laser beams into the main optical path of the microscope. The dichroic mirror is a good reflector for the two laser wavelengths (643 nm and 680 nm), but it is also a good transmitter for most of the rest of the white-light spectrum. The camera can thus see the white-light-illuminated sample quite clearly through this dichroic mirror. The microscope's polarizer and analyzer are needed for polarization microscopy of MO samples.

2.1 Laser Diodes

Shown at the lower left side of Fig. 1 are two laser diodes. The beams from both lasers are linearly polarized parallel to the plane of the figure (p-polarization). Each laser can be operated either in cw or in pulsed mode. In the cw mode the power P_1 of laser 1 can be adjusted continuously from 0 to 20 mW. Laser 2 has a cw power range from 0 to 30 mW. In the pulsed mode, both lasers can be switched with less than 5 ns rise and fall times. The maximum pulse power output of laser 1 is 40 mW; that from laser 2 is 50 mW. Both lasers have been fitted with collimating and circularizing optics. The aforementioned values of the optical power represent the lasers' raw output; the actual power available after collimation and beam shaping is only 78% of the raw power for both lasers. A feedback circuit is built into both laser drivers to maintain their cw outputs at a constant level. The feedback signal is provided by a small polarizing beam-splitter cube mounted in front of each laser diode package, which diverts ~1% of the beam to a detector in the feedback loop. Unfortunately, for the pulsed mode such feedback control of the output power is at present unavailable. Consequently, the optical pulse power drifts slightly during the experiments, and the results of measurements need to be corrected for this variation of the laser power during the recording cycle.

The collimated and circularized beams emerging from lasers 1 and 2 are approximately 4 mm and 5 mm in diameter, respectively. Wave-front analysis by shearing interferometry indicates that both beams are highly collimated and substantially free from aberrations, although the beam from laser 2 exhibits a small amount (~ 0.25λ peak-to-valley) of astigmatism. The beams from the two laser diodes are combined at a multilayer stack specifically designed to reflect the 680 nm line and to transmit the 643 nm line. The beam combiner transmits ~ 90% of the beam from laser 1 and reflects 98% of the beam from laser 2 toward the sample.

2.2 Leaky Polarizing Beam-splitter

The combined beams, now collinear and having the same p polarization (i.e., E-field parallel to the plane of Fig. 1), enter a leaky polarizing beam splitter (LPBS). The LPBS transmits 80% of the incident p-polarized light's power, reflecting the remaining 20%, which, in the forward path, is wasted. In the return path the LPBS behaves the same way, reflecting only 20% of the incident p-polarized beam toward the half-wave plate. However, the reflectance of the LPBS for s-polarized light (E-field perpendicular to the plane of Fig. 1) is nearly 100%. This is important for MO samples, because the MO signal is essentially contained in the s-component of the reflected polarization. In the return path this s-component is fully reflected at the LPBS and reaches the detectors. Only 20% of the returning p-component from the sample goes to the detectors at this point, but the p component is needed only as a reference signal for heterodyne detection—the p component does not contain any MO information—and, therefore, no major losses occur at the LPBS. In the case of PC and WORM samples, the liquid-crystal (LC) cell described below converts the incident p-polarized light into circular polarization and, in the return path, converts the circularly polarized beam reflected from the sample into s-polarized light. Because the LPBS reflects nearly 100% of this s-polarized light toward the detectors, there are no significant losses of the optical power in the case of PC and WORM samples either.

All types of recordable and rewritable media (WORM, PC, MO) that are available at present require several milliwatts of laser power incident upon the sample in order to reach temperatures that are high enough for crystallization or melting (PC, WORM) or for magnetization reversal (MO). Given the low transmission efficiency of high-NA objectives – due to mismatch between the size of the laser beams and the objectives' clear aperture – it is imperative to design the rest of the optical path for maximum throughput. In our system, in the forward path the LPBS transmits ~80% of the power of each laser toward the microscope objective. The LC cell is antireflection coated and has a transmission efficiency of better than 90%, and the dichroic mirror reflects 90% of the 643 nm beam and essentially all of the 680 nm beam.

2.3 Liquid Crystal Phase Retarder

After the LPBS, in the forward path the system contains a LC retarder. For MO applications this retarder is oriented with its fast and slow axes parallel and perpendicular to the direction of incident polarization. In the incident path the polarization, being linear and parallel to one of the axes of the LC cell, is not affected by this device. In the return path, however, the LC introduces a controlled phase shift between the *p*- and *s*-components of polarization. The polarization ellipticity induced in the beam by the MO sample and its substrate, if any, as well as all differential phase retardations introduced elsewhere in the system (e.g., at the dichroic mirror) can therefore be corrected by adjustment of the relative phase shift $\Delta\Phi$ of the LC cell. All one needs to do in this case is adjust the voltage control knob on the cell's controller unit to maximize the differential MO signal obtained at the detectors.

For the testing of PC and WORM media we set the relative phase delay $\Delta\Phi$ of the LC cell to nearly 90°, then rotate the cell about the optical axis until its fast and slow axes are oriented at ±45° with respect to the direction of incident polarization. Of course, it is impossible to adjust $\Delta\Phi$ simultaneously for both wavelengths, but because λ_1 and λ_2 are close to each other, one can get nearly circular polarization for both beams out of the LC cell. In the return path the same $\Delta\Phi$ acts on the reflected beams to convert their nearly circular polarization into nearly linear *s*-polarization (i.e., perpendicular to the plane of Fig. 1). After transmission through the LC cell in the return path, both *s*-polarized laser beams will be diverted by the LPBS toward the detectors.

A complicating factor in the case of PC and WORM media testing is the undesirable phase shift between r_p and r_s, the *p*- and *s*-reflectivities of the dichroic mirror. Ideally, the dichroic mirror must be designed to introduce no phase difference between r_p and r_s for either laser wavelength. The dichroic mirror used in our system, however, is an off-the-shelf item, which is not optimized in this respect. If there is a phase difference between r_p and r_s of this mirror, it causes a departure from circular polarization of the beam incident upon the sample; moreover, in the return path it causes a reduction of the total fraction of the reflected light that would ultimately reach the photodetectors. In practice, we adjust the orientation angle as well as the retardation $\Delta\Phi$ of the LC cell to minimize the back-reflections from the sample into the lasers while maximizing the detectors outputs. Typically, a couple of degrees of rotation of the LC cell and a slight adjustment of $\Delta\Phi$ are all that it takes to eliminate the back-reflections. (We estimate the dichroic mirror's phase retardation to be less than 10°.) In any event, this retardation does not cause any serious difficulties in our measurements, because the polarization state of the focused spot is inconsequential in read–write experiments on PC and dye–polymer media; moreover, as far as back-reflections into the lasers are concerned, the aforementioned adjustments readily solve the problem.

2.4 Translation Stage

The sample sits atop an XY translation stage, which can move under computer control in the horizontal plane in steps of 0.1 μm by as much as 70 mm along both X and Y axes with better than ± 1.0 μm repeatability. This feature is used for scanning optical microscopy of the samples. The controlled movement of the stage is also used in experiments that require repeated measurements of the same physical quantity at different locations of the sample. In such experiments the sample moves to a new location for a fresh measurement; then the results are averaged over repeated measurements to reduce the effect of random noise. For example, in some of the measurements described in sections 3 and 4, an array of 40 marks was recorded sequentially, and the reported results are averages over these 40 points.

2.5 Electromagnet

Placed under the sample's stage is an electromagnet that provides the necessary magnetic field during MO measurements. The 5 mm-diameter tip of the magnet's conical pole piece is centered directly under the focused laser spots. [Not shown in Fig. 1– but important for obtaining a large magnetic field at the sample – is an arm made from the same material (iron) as the magnet's core. The arm, attached to the bottom of the core and extending all the way to the top of the XY stage, provides a path of least resistance for the magnetic field, thus helping to concentrate the field in the small air gap just above the conical pole piece. Drilled in the upper end of this magnet's arm is a small hole that allows the focused beams of light to get through to the sample.] The maximum current supplied to the coil is ± 5.0 A, yielding a maximum magnetic field $H_{max} = \pm 8.1$ kOe in the plane of the sample (which is also the focal plane of the objective lens).

At room temperature ($T_{ambient} \approx 20$ °C) the electrical resistance of the coil is 5.6 Ω, but it changes with time as the coil's temperature rises. For this reason the magnetic field is adjusted by computer control of the electrical current (rather than voltage) supplied to the coil. A complete loop scan of the field between $\pm H_{max}$ takes anywhere from several ten seconds to a few minutes, depending on the chosen step size ΔH for the magnetic field.

2.6 Detection Module

The beam reflected from the sample returns through the LC cell to the LPBS and is directed toward the detectors. As mentioned earlier, the LPBS reflects nearly 100% of the *s*-polarized light and only 20% of the *p*-polarized light toward the detection module. The first element in the return path after the LPBS is the half-wave plate (HWP), whose bandwidth is wide enough to make it an accurate HWP for both $\lambda_1 = 643$ nm and $\lambda_2 = 680$ nm. In MO applications, the HWP is used to rotate the polarization until the light is nearly equally split between the two detection channels. For PC samples the HWP is not necessary, but it may be used to control the amount of light that enters the desired channel. The polarizing beam

splitter immediately after the HWP sends the component of polarization parallel to the plane of the diagram straight through, but it reflects the perpendicular polarization toward the channel on the left.

The two beams exiting the polarizing beam splitter go through identical prisms, the dispersion of which is large enough to separate the two wavelengths. Emerging from each prism are two beams with wavelengths λ_1 and λ_2 that have an angular separation of ~0.28°. In each channel a 63.5 mm focal-length lens focuses the two beams on the separate halves of a split photodetector. (This is actually a quad detector, in which each individual rectangular detector is 300 μm × 600 μm in size, and the gap-width between adjacent cells is 10 μm. We use only two of the four detectors in each channel, choosing the diagonal pair for maximum separation and minimum cross-talk.) The focused spots are ~25 μm in diameter, and their center-to-center spacing is ~300 μm.

We thus collect four signals, S_{p1}, S_{p2}, S_{s1}, S_{s2}, out of the two split-detectors. Here the subscripts *s* and *p* refer to the state of polarization of the beam that emerges from the HWP, and the subscripts 1 and 2 refer to wavelengths λ_1 and λ_2, respectively. The individual detectors have an efficiency $\eta \sim 0.5$ mA/mW. The gain of the amplifiers for the detectors of the λ_1 line is $G_1 = 50$ V/mA; that of the λ_2 line is $G_2 = 14$ V/mA; all the amplifiers have a 160 MHz bandwidth. By forming the various sums and differences of the electronic signals one obtains the total reflectance of the sample as well as the differential MO signal. (The reflectances of the various samples are calibrated against a polished silicon surface.) For PC and WORM measurements we usually adjust the HWP to send all the light through the polarizing beam splitter. In this case S_{p1} is proportional to the reflectivity of the sample at λ_1 and S_{p2} represents the reflectivity at λ_2. For MO measurements, the fast (or slow) axis of the HWP is rotated by 22.5° from the plane of Fig. 1, sending equal amounts of the two components of polarization to each detector. In this case the normalized differential signals are $(S_{p1} - S_{s1}) / (S_{p1} + S_{s1})$ for λ_1 and $(S_{p2} - S_{s2}) / (S_{p2} + S_{s2})$ for λ_2. The normalized differential signals are proportional to the polarization rotation angle at the sample (i.e., Kerr angle in the case of MO media), but one must be careful to account for the reduced value of the *p*-component of polarization at the LPBS.

2.7 Calibration

We performed several measurements on aluminized mirrors and on polished silicon substrates to calibrate the system. Both aluminum and silicon have high thermal conductivities and, therefore, the laser beams were not expected to create substantial temperature gradients in them. We used the reflected light from these calibration samples to determine the temporal shape of the laser pulse, and to establish the relationship between the measured voltage at the detectors and the actual reflectance of the sample. We also measured the cross-talk between adjacent detectors and found it to be at acceptable levels.

3. Measurements on Phase-change Media

These measurements were conducted on four different quadrilayer samples depicted schematically in Fig. 2, and listed in Table 1. The laser beams were focused on the PC layer through the sample's substrate, and the 0.6NA microscope objective used in the experiments was corrected for the substrate thickness. The PC layers in all the samples studied were initially in the as-deposited amorphous state.

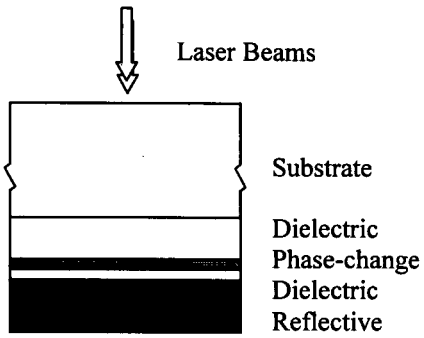

Fig. 2 Typical quadrilayer stack consisting of a PC layer sandwiched between two dielectric layers and capped by an aluminum-alloy reflective layer.

Table 1. Characteristics of PC samples used in the experiments

	S_1	S_2	S_3	S_4
Substrate	Glass (1.2 mm)	Polycarbonate (1.2 mm)	Polycarbonate (0.6 mm)	Glass (1.2 mm)
Dielectric	ZnS-SiO_2 (77 nm)	ZnS-SiO_2 (68 nm)	ZnS-SiO_2 (68 nm)	ZnS-SiO_2 (60 nm)
Phase change	$Ge_2Sb_{2.3}Te_5$ (25 nm)	$Ge_2Sb_{2.3}Te_5$ (25 nm)	$Ge_5Sb_{68}Te_{27}$ (16 nm)	AgInGeTe (21 nm)
Dielectric	ZnS-SiO_2 (25 nm)	ZnS-SiO_2 (155 nm)	ZnS-SiO_2 (20 nm)	ZnS-SiO_2 (28 nm)
Reflective	Al-alloy (100 nm)	Al-alloy (100 nm)	Al-alloy (200 nm)	Aluminum (130 nm)

Fig. 3 shows a small section of sample S_1 as seen by the CCD camera through the microscope. The bright rectangular region ($R \sim 15\%$) on the dark background ($R \sim 2\%$) represents a fully crystallized section of the PC film. This region was prepared by slow XY scanning of the as-deposited amorphous film under a cw laser beam ($P_2 = 2.5$ mW). In the large crystalline region, a 5 × array of melt-quenched amorphous marks was written by pulsing laser 1 at $P_1 = 14.0$ mW, $\tau = 0.1$ μs. Also seen in Fig. 3 are crystalline marks written on the as-deposited region of the sample. These marks were written by pulsing laser 2 at $P_2 = 4.0$ mW, $\tau = 1.0$ μs (left-hand side of the figure) and $P_2 = 5.0$ mW, $\tau = 1.0$ μs (right-hand side). The center-to-center spacing between adjacent marks is 5.0 μm. Detailed crystallization/amorphization experiments on this sample were reported in our earlier publications.[1-5]

3.1 Sb-rich Sample

Figure 4 shows results of a crystallization experiment on sample S_3. In this experiment laser 2 was pulsed at P_2 = 10 mW, $\tau = 1.5$ ms, while laser 1 operated cw at $P_1 = 0.2$ mW. P_1 is sufficiently weak that its thermal effect on the

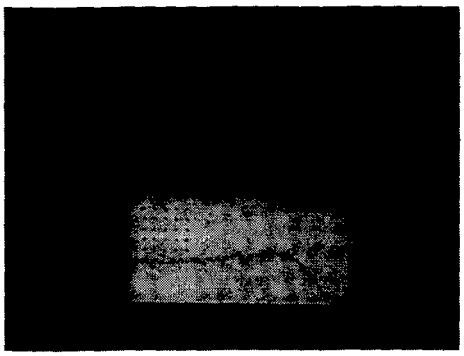

Fig. 3 Photograph of a small section of sample S_1, as seen through the microscope by the CCD camera. Bright and dark areas represent crystalline and amorphous regions of the phase-change film, respectively.

sample may be ignored. The curves in Fig. 4 show the measured reflectivity variations during four crystalline-mark-formation attempts at different points under identical pulse powers. The lower curve corresponds to a failed attempt, in which R started at ~ 1.5% and, with the onset of laser pulse at t = 0, increased to 6%, where it stayed until the end of the pulse at t = 1.5 ms. Thereafter, R returned to its amorphous-state value of ~ 1.5%. This rise and fall in R are believed to be due to a reversible change of the optical constants of the PC layer with temperature. The remaining three curves represent crystalline-mark formation at three different points of time during the pulse, as evidenced by an abrupt increase of R from ~ 6% to ~ 20% in the corresponding traces. This random-looking crystallization behavior is uniquely associated with the non-stoichiometric composition of the PC layer in sample S_3. In contrast, our crystallization studies on S_1, in which the PC layer is stoichiometric, showed a deterministic behavior.[2), 3)]

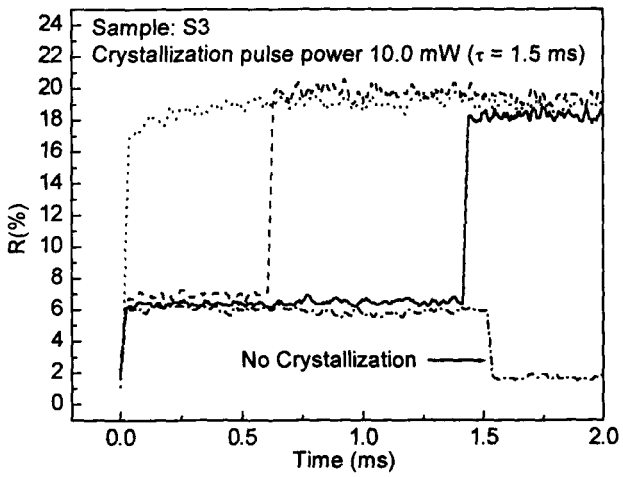

Fig. 4 Temporal variations of reflectivity during local crystallization of the as-deposited amorphous PC film of S_3. The pulse from laser 2 (P_2 = 10.0 mW, τ = 1.5 ms) extends from t = 0 to 1.5 ms.

3.2 Melting and Amorphization

An example of reflectivity variations during melt-quenched amorphous-mark-formation is shown in Fig. 5. A large area of S_1 was initially crystallized, using the computer-controlled scanning capability of the translation stage and the 680 nm laser at the cw power of P_2 = 2.0 – 3.0 mW. Afterwards amorphous marks were recorded in this crystallized area by pulsing laser 2 for τ = 0.1 μs at several pulse powers (P_2 = 8.0 – 14.0 mW). Laser 1, operating cw at 0.2 mW, was used to monitor the local melting and quenching of the sample.

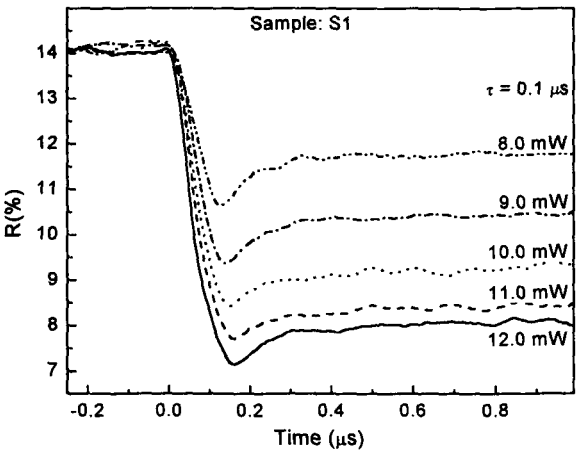

Fig. 5 Temporal variations of reflectivity during localized melting and subsequent quenching of the pre-crystallized PC film in S_1 under pulsed beam from laser 2 at various pulse powers. (The pulse extends from t = 0 to t = 0.1μs.)

The initial reflectivity R before the start of the pulse at t = 0 is ~ 14.0 %. With the onset of the pulse, R begins to decrease. Some of the initial drop in R (before T reaches the melting point) is due to the changing optical constants of the media with temperature. The reflectivity drop continues with the onset of melting until the end of the pulse. The net drop in R increases with increasing pulse power as the onset of melting occurs earlier for larger pulse powers. Therefore, the rate of drop of R – or the net drop in R during the pulse – increases with increasing pulse power. At higher pulse powers, of course, the size of the molten pool is larger, and a larger drop in R is expected. It is interesting to note that, at high pulse powers, R continues to drop even after the end of the pulse. This drop in R may be due to the quenching of the molten pool, indicating a difference between the optical constants of amorphous and melt states of the sample.

3.3 Is Erasure Nucleation or Growth Dominated?

Since the achievable data-rates in PC recording are limited by the speed at which amorphous marks can be erased (re-crystallized) during overwrite, it is important to compare the erasure behavior in various classes of PC media. We noted earlier that the crystallization behavior of $Ge_5Sb_{68}Te_{27}$ (sample S_3) appears to be random compared to that of $Ge_2Sb_{2.3}Te_5$ (sample S_1).[2), 3)] This and other observed differences among the various media formulations are believed to be due to the differences in nucleation/growth probabilities of crystallization kinetics.

Samples S_1, S_3 and S_4 have three different types of PC

material, for which we wish to examine the erasure process under static conditions. To this end, we crystallized large areas of each sample by the scanning method described earlier, then recorded amorphous marks using 0.1 μs pulses from laser 2 at various power levels. These marks were subsequently re-crystallized, and their erasure times were correlated with their sizes.

Figure 6 shows the results of one such experiment conducted on S_1. Amorphous marks of differing sizes were created by focusing laser 2 on a pre-crystallized film at various pulse powers (P_2 = 9, 10, 12, and 14 mW). These marks were re-crystallized under P_2 = 14 mW, τ = 4 ms pulses from a defocused laser 2, while focused laser 1 (cw) monitored the process. Defocusing of laser 2 produces a fairly large optical spot over the (relatively small) amorphous mark, which ensures uniform temperature distribution at and around the mark location. (Since the mark is smaller than the focused spot of laser 1, its initial reflectivity conveys its size. Thus a lower initial reflectivity in Fig. 6 means a larger amorphous mark.) It is evident in Fig. 6 that erasure starts slightly before t = 0.5 ms for all mark sizes. In the beginning, there is rapid erasure, but it slows down in time. Towards the end of the pulse, all reflectivity traces converge to $R \sim$ 14.25%, which is the crystalline-state reflectivity of the sample. This indicates a unique value for the erasure time for different-sized amorphous marks.

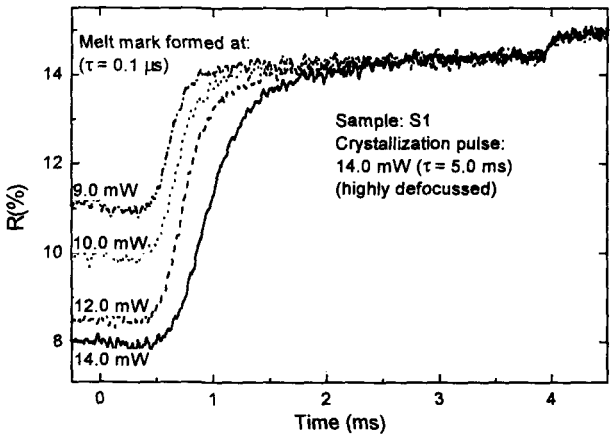

Fig. 6 Reflectivity variations during the erasure of melt-quenched amorphous marks of differing sizes in sample S_1. The marks were recorded on the pre-crystallized film using 14, 12, 10 and 9 mW pulses (τ = 0.1 μs). Erasure was achieved using a defocused beam from laser 2 (P_2 = 14 mW, τ = 4 ms). The process was monitored by the cw beam from laser 1 (P_1 = 0.2 mW).

Similar experiments were conducted on samples S_3 and S_4, with the results appearing in Figs. 7 and 8, respectively. These recrystallization curves differ in two respects from those of Fig. 6. A slight drop in R in the beginning of the erasure pulse may be associated with the temperature-dependence of the optical constants of the PC layer. However, the most important observation about these samples is that their reflectivity traces do not converge simultaneously to the sample's crystalline-state reflectivity. Instead, each trace reaches saturation at a different point in time, with the trace that starts from a higher initial value (i.e., smaller amorphous mark), reaching saturation earlier than the one which starts at a lower initial reflectivity. This behavior is indicative of a mark-size dependence of the erasure time in S_3 and S_4.

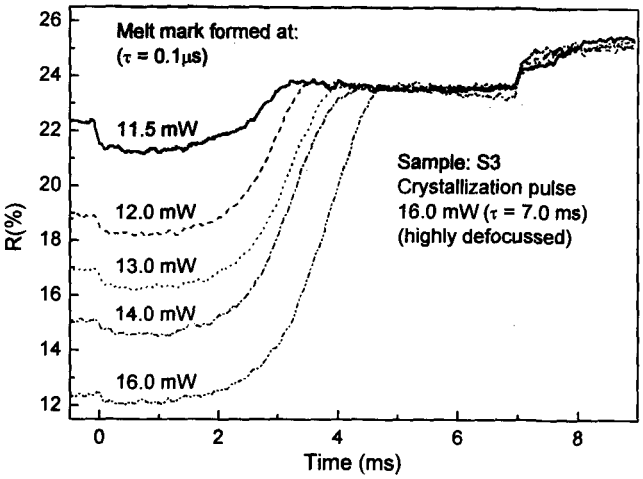

Fig. 7 Reflectivity variations during erasure of melt-quenched amorphous marks of differing sizes in S_3. The marks were created by P_1 = 16, 14, 13, 12 and 11.5 mW, τ = 0.1 μs pulses on the pre-crystallized PC film. Erasure was carried out by a defocused 16 mW, τ = 7 ms pulse from laser 2, and monitored by laser 1 operating cw at P_1 = 0.2 mW.

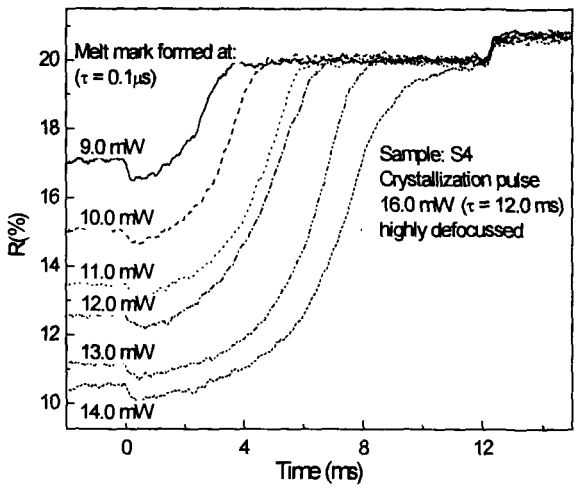

Fig. 8 Reflectivity variations during erasure of melt-quenched amorphous marks of differing sizes in S_4. The marks were recorded using P_2 = 14, 13, 12, 11, 10 and 9 mW, τ = 0.1 μs pulses on a pre-crystallized film. Erasure was carried out by a defocused 16 mW, τ = 12 ms pulse from laser 2, and monitored by laser 1 operating cw at P_1 = 0.2 mW.

3.4 Temperature-dependence of Optical Constants

Figure 9 shows reflectivity variations in sample S_2 under the influence of two consecutive, identical 0.1 μs pulses from laser 2, separated by ~4.0 μs. (The two pulses are applied during t = 0.0 - 0.1 μs and t = 4.15 - 4.25 μs.) In this experiment the laser power was varied

from 2 mW to 8 mW when the PC layer was in the as-deposited amorphous state (lower set of four curves) and, from 2 mW to 10 mW when the PC film was in the pre-crystallized state (upper set of four curves). In the as-deposited amorphous state, reflectivity variations are fully reversible for pulse powers in the range of 2 – 5 mW. Reflectivity starts increasing with the onset of the pulse as it heats up the PC film, and continues to increase for as long as the pulse is in effect. Upon removing the pulse, R returns to its amorphous-state value as the film cools down. This pattern of behavior is exhibited during both the initial and the subsequent pulse. Upon increasing the pulse power beyond 5 mW, we notice that much of the gain in R is reversed at the end of the first pulse. However, during the second pulse there is a significant permanent increase of reflectivity due to the formation of a crystalline mark. It is interesting to note that a 7 mW first pulse does not induce much crystallization, whereas an identical second pulse applied 4 μs later could make a fairly large crystalline mark. The first pulse, therefore, modifies the state of the PC film to "primed amorphous," which exhibits rapid crystallization upon the application of the second pulse. This behavior has been discussed in detail in our earlier publications.[3), 5)]

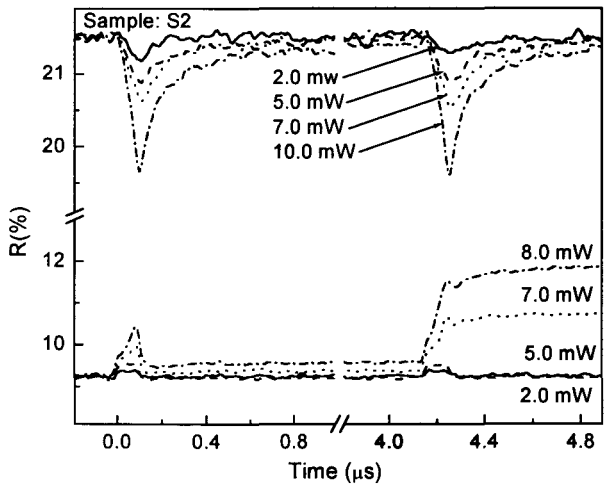

Fig. 9 Variations of reflectivity upon the application of a pair of identical pulses (τ = 0.1 μs, separated by 4.0 μs) to sample S_2 on its crystalline (upper set of curves) and as-deposited amorphous (lower set) regions. The pulses occur during the intervals 0 - 0.1 μs and 4.15 - 4.25 μs.

The reversible nature of the variations of R can also be noticed in the upper set of curves in Fig. 9, where reflectivity drops with the onset of the pulse, and goes back to its crystalline-state value after removing the pulse. However, this reversible behavior cannot be completely associated with temperature dependence of the optical constants for all pulse powers. At higher powers the temperature at the center of the focused spot exceeds the film's melting point, leading to the formation of a molten pool and, therefore, a drop in R. Under such circumstances, one expects a net drop in R due to the presence of a melt-quenched mark at the end. However, in S_2 the dielectric layer separating the PC and the aluminum layers is fairly thick (155 nm), causing slow cooling and subsequent crystallization of the melt, thus bringing R back to its crystalline-state level upon the termination of the pulse.

4. Measurements on Magneto-optical Media

In this section we present results of various measurements on a quadrilayer MO sample deposited on a glass substrate. The 25nm-thick magnetic layer is an amorphous alloy of TbFeCo having compensation point somewhat below the room temperature. Both dielectric layers are SiN, and the reflective layer is an aluminum alloy. The sample is initially saturated in a large magnet with a 21 kOe field. During these experiments the ambient temperature can be raised by placing a hot plate under the sample; thermal grease is applied to improve the contact between the sample and the hot plate.

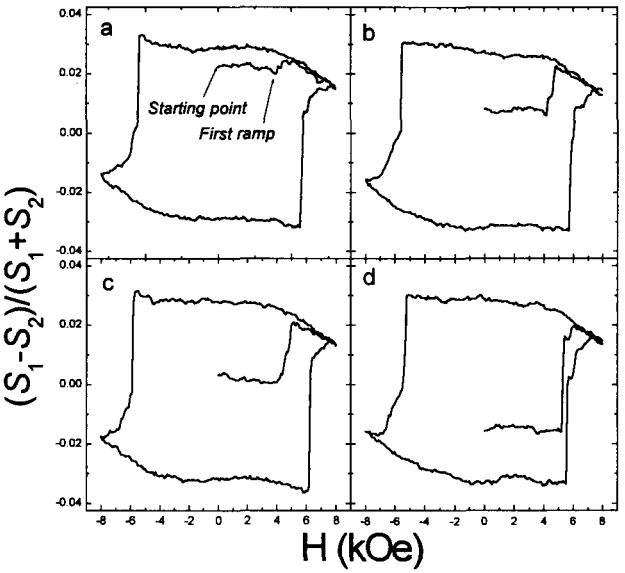

Fig. 10 Kerr hysteresis loops measured on recorded MO domains using laser 2 in cw mode (P_2 = 0.8 mW). The sample's magnetization is along +Z, and the recorded domains are magnetized along -Z. In (a) the initial domain is the smallest, and in (d) the largest. The first ramp in each case indicates the onset of contraction of the recorded domain.

4.1 Hysteresis Loops

Figure 10 shows hysteresis loops measured on a recorded domain within a quadrilayer MO sample. The sample was initially saturated with its magnetization along the +Z direction. A reverse domain was then written by pulsing laser 1 under a reverse magnetic field ($H < 0$, P_1 = 2 mW, τ = 2 μs). Subsequently, laser 2 was focused at the center of the written domain at cw power P_2 = 0.8 mW, and the hysteresis loop was traced. The loops in Figs. 10(a - d) correspond to domains written under different magnetic fields: H = -1.38, -2.45, -3.7, and -4.7 kOe. During loop-tracing, the first ramp encountered after the application of the magnetic field indicates the onset of contraction of the recorded domain. For small domains the field at which the first ramp occurs

is smaller than that for large domains, as shown in Figs. 10(a - d), which represent successively larger domains. The balance of the magnetic forces in this sample is such that a stronger field is required to shrink a larger domain.

4.2 Estimation of Thermal Conductivity

A laser beam is focused through the objective lens onto the stationary MO sample. With the increasing cw laser power P, the local temperature T in the MO film increases, causing changes in the monitored differential signal ΔS. At a critical power P_c, the peak temperature (at the center of the focused spot) reaches the Curie temperature T_c. Once P_c and T_c are determined, one can proceed to estimate the thermal conductivities of the various layers by comparing the experimental data with results of thermal simulations.

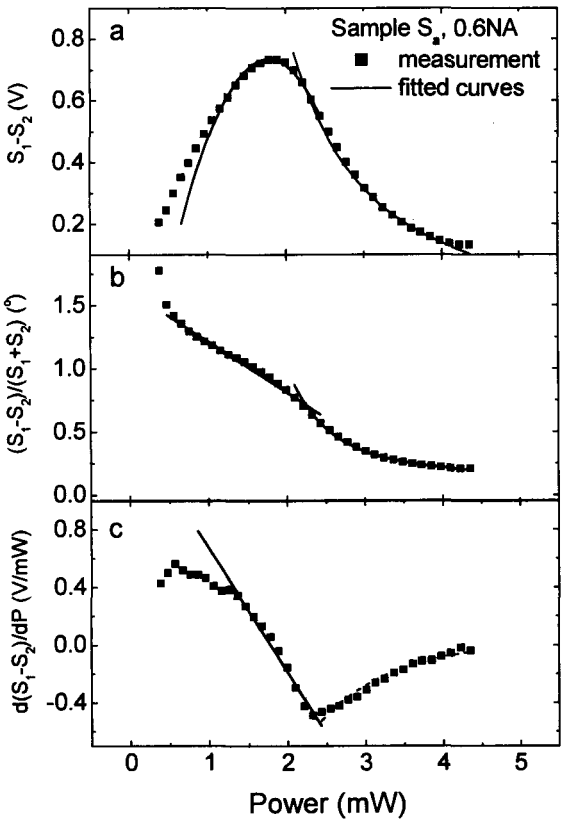

Fig. 11 Experimental data from a quadrilayer MO sample obtained at 0.6NA at the ambient temperature of 20°C. (a) ΔS, (b) $\Delta S/(S_1 + S_2)$, (c) $d\Delta S/dP$. The data are fitted with a theoretical model (solid lines) to show their consistency.[6] The minimum point in (c) corresponds to $P_c = 2.32$ mW.

Figure 11 shows the measured results on an MO sample at the ambient temperature of 20°C using a 0.6NA objective. The data are fitted with a theoretical model, and the resulting curves (solid lines) are also shown in the figure.[6] It is interesting to note that for $P > 1$ mW the theoretical results are consistent with the experimental data. For $P < 1$ mW the difference between theory and experiment may be ascribed to a departure from linear dependence of the Kerr angle on T. It is seen in Fig. 11 that ΔS and $\Delta S/(S_1 + S_2)$ change smoothly with P, while $d\Delta S/dP$ has a well-defined minimum at $P = 2.32$ mW. At this power the peak temperature in the MO film must have reached the Curie temperature T_c.

We used the hot stage to estimate T_c of the sample. When the sample's ambient temperature increases, P_c decreases. If the hot stage by itself could raise the temperature of the MO layer to T_c, the value of P_c would drop to zero. Therefore, one may obtain an estimate of T_c from the dependence of P_c on the ambient temperature.

Figure 12 shows plots of P_c versus the ambient temperature measured with 0.6NA, 0.4NA, and 0.25NA objectives. The data may be fitted with straight lines, as shown. These lines cross the horizontal axis at $T = 275.2$, 277.5, and 278.4°C, giving the estimated $T_c \approx 277 \pm 2$°C. (Since the maximum temperature of our stage is well below the estimated T_c, it was not possible to obtain a direct measurement of the Curie temperature.)

The knowledge of the Curie temperature T_c and of the critical power P_c at sevral different values of the objective's NA enables one to estimate the thermal conductivities of the various layers of the MO stack. The results are listed in Table 2. For a detailed description of these measurements, the interested reader is referred to our original paper on the subject.[6]

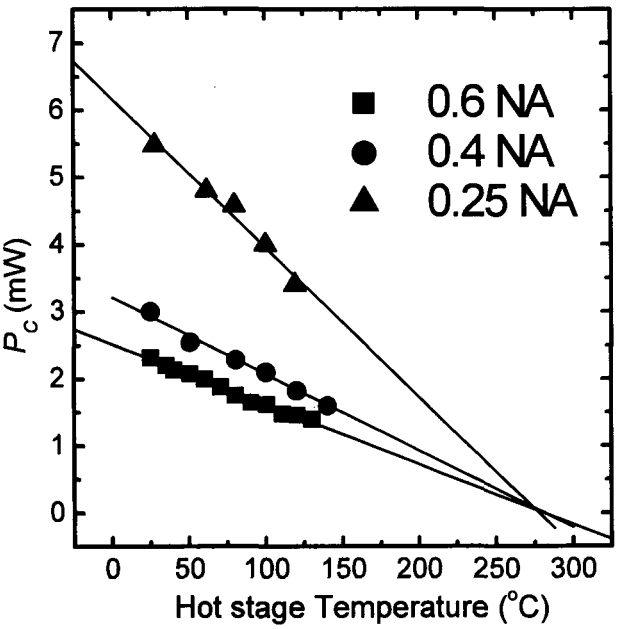

Fig. 12 Experimental data of the critical laser power P_c versus the ambient temperature, obtained with three different objective lenses on a quadrilayer MO sample. All three straight lines fitted to the data cross the horizontal axis at the Curie temperature $T_c \approx 277 \pm 2$°C.

Table 2. Refractive indices at $\lambda = 643$ nm and estimated thermal conductivities of MO media

	$n + ik$	K (W/cm/°C)
SiN	2.01	0.021 – 0.024
TbFeCo	3.25 + i 4.32	0.12 – 0.13
Glass Substrate	1.52	0.010

4.3 Magnetization Reversal Dynamics

Figure 13 shows variations of the MO Kerr signal obtained by pulsing laser 1 at $P_1 = 4$ mW, $\tau_1 = 2$ μs, and monitoring the sample with laser 2 operating cw at $P_2 = 0.3$ mW. Different curves correspond to different values of the applied magnetic field H. The sample was initially saturated along the -Z direction where the Kerr signal is negative. Each curve was obtained by averaging over 100 identical measurements.

At $H = -1.38$ kOe, the Kerr signal increases during the pulse, and returns to its original level after the pulse is turned off. This shows the thermal effect of the laser beam on the sample's magnetization, without reversing the magnetization direction at any point during the pulse. At $H = +0.3$ kOe, the signal is nearly the same as that at $H = -1.38$ kOe during the pulse, but it jumps to a higher value when the pulse is terminated. Magnetization reversal thus appears to take place during the cooling period. At higher magnetic fields, $H = 1.38$, 2.45, and 3.7 kOe, the signal's behavior is qualitatively similar, but the observed changes are greater.

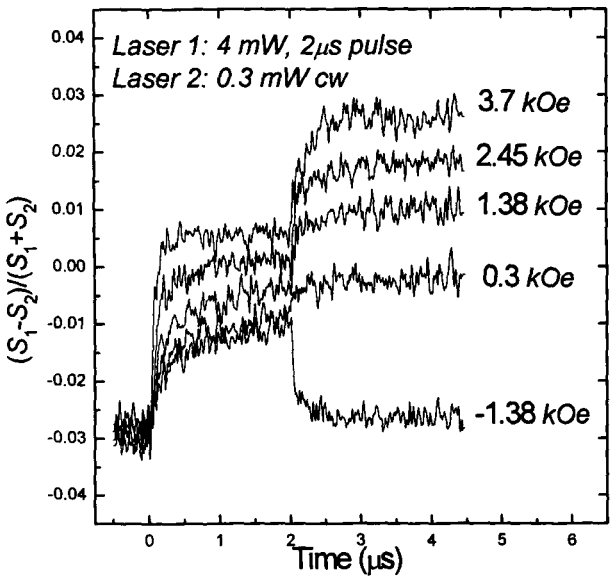

Fig 13. Variations of the Kerr signal from a quadrilayer MO sample in response to a $P_1 = 4$ mW, $\tau_1 = 2$ μs pulse from laser 1. Laser 2, operating cw at $P_2 = 0.3$ mW, monitors the process. The sample is initially magnetized along the –Z direction. Different curves correspond to different values of the applied field H, as indicated.

Because the magnitude of the Kerr effect decreases with the rising temperature, the differential signal in Fig. 13 increases (from its initial negative value) during the pulse. At $H = +0.3$ kOe, the increased signal level at the end of the pulse (i.e., beyond $t = 2$ μs) indicates that some of the magnetic moment of the sample has been reversed, although this reversal is not seen during the heating cycle. The reason is that, in the central region under the focused spot, T exceeds T_c during the pulse, leaving no magnetization in this region and contributing no Kerr signal. When the pulse is turned off, the magnetization in the central region re-appears, this time along +Z, leading to a positive jump in the Kerr signal at $t > 2$ μs. Thus the total Kerr signal has contributions from three regions: (i) the central region under the focused spot, which, when above T_c, contributes no signal; (ii) a ring surrounding the central region, having magnetization along +Z and contributing a positive signal; (iii) the unreversed region outside the ring (i.e., the rest of the sample), having magnetization along -Z and contributing a negative signal. The behavior of the Kerr signal under different magnetic fields shown in Fig. 13 may be readily explained if one takes into account the contributions from these three regions of the sample.

5. Summary

We have demonstrated the applicability of a general-purpose static-tester for measurements of the physical properties of various samples of recordable and rewritable optical storage media. The name static-tester implies that the sample is stationary while being recorded upon and read out. This is in contrast with the actual environment of a disk in an optical drive, where the medium has a velocity of several meters per second relative to the focused laser spot. Although for fundamental studies of media properties such static testing is adequate, conclusions about the dynamic environment within a disk drive require further elaboration, especially with regard to the effect of shifting thermal gradients introduced in a rapidly rotating disk.

Acknowledgements

The authors are grateful to Takeo Ohta and Kenichi Nagata of the Matsushita Electric Industries of Japan, Michikazu Horie of Mitsubishi Chemical Corp., Terril Hurst of the Hewlett-Packard Laboratories, Kelly Daly Flynn and David Strand of the Energy Conversion Devices, and Chung-Hee Chang of Seagate Media Research Center for providing the samples for this study, and for many helpful discussions. This work has been supported by the Optical Data Storage Center at the University of Arizona, and by a grant from the U.S. Department of Commerce's National Institute of Standards and Technology under the Advanced Technology Program (award number 70NANB7H3054).

References

I. M. Mansuripur, J. K. Erwin, W. Bletscher, P. K. Khulbe, K. Sadeghi, X. Xun, A. Gupta and S. B. Mendes, *Appl. Opt.* **38**, 7095-7104 (1999).

II. P. K. Khulbe, X. Xun and M. Mansuripur, *Appl. Opt.* **39**, 2359 (2000).

III. P. K. Khulbe, E. M. Wright and M. Mansuripur, *J. Appl. Phys.* **88**, 3926 (2000).

IV. E. M. Wright, P. K. Khulbe and M. Mansuripur, accepted for publication in *Applied Optics* (2000).

V. P. K. Khulbe, X. Xun and M. Mansuripur, Proceedings of International Symposium on Optical Memory and Optical Data Storage, SPIE Vol. **3864**, 211 (1999).

VI. X. Xun, C. Peng, and M. Mansuripur, *Appl. Opt.* **39** 4355-4360 (2000).